Simulation and optimisation of terahertz emission from InGaAs and InP photoconductive switches

J. Lloyd-Hughes*, E. Castro-Camus, M.B. Johnston*

Clarendon Laboratory, Department of Physics, University of Oxford, Parks Road, Oxford OX1 3PU, UK

Abstract

We simulate the terahertz emission from laterally biased InGaAs and InP using a three-dimensional carrier dynamics model in order to optimise the semiconductor material. Incident pump-pulse parameters of current Ti:Sapphire and Er:fibre lasers are chosen, and the simulation models the semiconductor's bandstructure using parabolic Γ, L and X valleys, and heavy holes. The emitted terahertz radiation is propagated within the semiconductor and into free space using a model based on the Drude–Lorentz dielectric function. As the InGaAs alloy approaches InAs an increase in the emitted power is observed, and this is attributed to a greater electron mobility. Additionally, low-temperature grown and ion-implanted InGaAs are modelled using a finite carrier trapping time. At sub-picosecond trapping times the terahertz bandwidth is found to increase significantly at the cost of a reduced emission power.
© 2005 Elsevier Ltd. All rights reserved.

1. Introduction

The ability to create and detect single-cycle pulses of coherent terahertz (THz) radiation has enabled diverse studies in condensed matter physics. Recent examples include a study of how surface plasmon polaritons propagate on semiconductor gratings [1], determining the low-energy vibrational modes of oligomers [2], and measuring the time-dependent intersubband absorption in semiconductor quantum wells [3]. Such studies have become possible using high power, broadband THz radiation emitters based on the ultrafast separation of photoexcited carriers in a photoconductive switch [4]. In this communication, we investigate how the choice of semiconductor alters THz emission,

by employing a carrier dynamics simulation to model InGaAs and InP photoconductive switches.

The use of a low-bandgap semiconductor (such as $In_{1-x}Ga_xAs$ with an alloy fraction $x \leq 0.47$) would enable cheaper, more stable, turnkey THz spectroscopy setups based on erbium fibre (Er:fibre) lasers, which can produce pulses as short as 65 fs at a central wavelength $\lambda = 1.55~\mu m$ [5]. Combining a compact system of this type with communications wavelength optical fibres would enable THz pulses to be generated and detected in small, extreme, or otherwise inaccessible environments (e.g. in an endoscope or in the cavity of a pulsed magnet).

While GaAs-based photoconductive switch technology is well developed [6], there are fewer InP and InGaAs-based THz emitters described in the literature [7–11]. Baker et al. [9] reported THz emission up to 3 THz from a low-temperature (LT) grown $In_{0.3}Ga_{0.7}As$ photoconductive switch, using a Nd glass laser. Additionally, Suzuki and

---

* Corresponding authors.

E-mail addresses: j.lloyd-hughes@physics.ox.ac.uk (J. Lloyd-Hughes), m.johnston@physics.ox.ac.uk (M.B. Johnston).

Tonouchi [10] have measured the THz emission from photoconductive switches made from $In_{0.53}Ga_{0.47}As$ implanted by 340 keV, 1×10^{15} cm^{-2} Fe ions. They used an Er:fibre laser with central wavelength 1.56 μm and pulse duration 300 fs, and measured THz power up to ∼2 THz. Finally, Mangeney et al. [11] performed a similar experiment on $In_{0.53}Ga_{0.47}As$ implanted by Au$^+$ ions, with a carrier lifetime of 0.9 ps.

In order to investigate suitable semiconductors for photoconductive switch THz emitters it is beneficial to adopt a modelling approach. The effect of altering one parameter (or more) of the semiconductor material or laser can be investigated rapidly, and an optimum combination sought. While analytical models of THz emission are relatively straightforward to interpret, they often require phenomological assumptions (e.g. about carrier mobilities). In this paper we, therefore employ a three-dimensional semi-classical carrier dynamics simulation to model $In_{1-x}Ga_xAs$ and InP photoconductive switch THz emitters.

2. Simulation details

The carrier dynamics model used herein is an extension of one used previously to model the THz emission from InAs and GaAs surfaces under a magnetic field [12], ion-implanted GaAs surfaces [13] and GaAs photoconductive switches [14]. A set of 10^6 pseudoparticles comprising extrinsic and photogenerated carriers and fixed ions are used to simulate the semiconductor. At each 5 fs step in time the model numerically finds the three-dimensional potential due to the charge density, subject to the appropriate boundary conditions for the surface and Schottky photoconductive switch contacts. Carrier–carrier, carrier–phonon and carrier–impurity scattering mechanisms are included [12]. The simulated particles are within a box of size $x \times y \times z = 6 \times 6 \times 4$ μm^3, subdivided into a grid of $64 \times 64 \times 32$. The contacts of the photoconductive switch are at $-3 \leq x \leq -1$ μm and $1 \leq x \leq 3$ μm. A constant bias voltage of 5 V between electrodes was used throughout this work, which corresponds to typical experimental field strengths. The simulation starts at a time $t = -0.7$ ps, to allow the extrinsic carriers to equilibrate before the arrival of the incident pulse, which has peak intensity at time $t = 0.0$ ps, and is centred at $x, y = 0$.

Although the simulation assumes a parabolic band structure for simplicity, in the modelling of THz emission from narrow band-gap semiconductor surfaces the inclusion of the L-valley was found to create a more realistic distribution of carrier energies [12]. In photoconductive switches the average carrier energy is greater than for surface emitters, and intervalley (e.g. $\Gamma \rightleftharpoons L$) scattering by absorption or emission of an optical phonon becomes more significant. Further, in the range $0.4 \lesssim x \lesssim 0.7$ the X-valley energy gap of $In_{1-x}Ga_xAs$ falls below that of the L-valley.

The simulation was, therefore, extended to include the X valley in addition to the Γ and L valleys.

2.1. Properties of InGaAs

Values of semiconductor parameters for $In_{1-x}Ga_xAs$ at a particular alloy fraction x were generated automatically within the simulation from the bowing parameter [15,16]. When no bowing parameter was found in the literature, linear interpolation between InAs and GaAs was used. The two-mode TO phonon energies for InGaAs of Ref. [17] were employed. For consistency the intervalley deformation potentials were taken from Ref. [18], the only reference found with values for GaAs, InAs and InP.

An inspection of the properties of InGaAs suggests potential advantages and disadvantages as a THz emitter when compared with GaAs. Firstly, a lower Γ-valley effective mass should result in a higher electron mobility, and greater THz power. Secondly, the intervalley deformation potential $D_{\Gamma-L}$ is greater for InAs than GaAs [18], resulting in a larger intervalley scattering rate. When electrons scatter to the L or X valley they lose kinetic energy, contributing to the deceleration of carriers that produces the negative peak in E_{THz}. The lower absorption coefficient of InGaAs at 1.55 μm compared with GaAs at 800 nm (0.8 and 1.2×10^6 m^{-1} respectively) is a disadvantage, because a lower α results in a lower bandwidth for defect-laden semiconductors, owing to the photogeneration of fewer carriers within the damaged depth. In addition, with a smaller α the emitted THz radiation will on average travel further through the semiconductor (when the reflection geometry [6] is used), and will be more significantly affected by absorption and dispersion.

Finally, since $In_{1-x}Ga_xAs$ exhibits two-mode TO phonon behaviour [17] the THz emission spectra should exhibit strong absorption peaks near the TO phonon energies (e.g. for $x = 0.47$ the two modes have frequencies of 6.8 and 7.6 THz). This will limit the spectroscopic use of $In_{1-x}Ga_xAs$ photoconductive emitters in the frequency range near and between the TO phonon modes of InAs and GaAs (6.4 and 8.1 THz). The following section describes how the two-mode TO phonon–polariton dispersion of InGaAs was included in the simulation.

2.2. THz propagation within photoconductive switch

The radiated THz electric field E_{THz} was calculated in the far-field approximation from the simulated current density $\mathbf{J}$ using the relation $\mathbf{E}_{THz} \propto (1 + \sqrt{\varepsilon})^{-1} \partial \mathbf{J}/\partial t$ [19], where the dielectric function ε was modelled using the well-known Drude–Lorentz formula for TO phonon–polaritons [20], which for two TO phonon modes is

given by:

$$\varepsilon_{\text{TO}}(\omega, x) = \varepsilon_\infty^x + \frac{\varepsilon_s^x - \varepsilon_s^{x=1}}{1 - \omega^2/\omega_{x=0}^2 - i\omega\Gamma/\omega_{x=0}^2}$$

$$+ \frac{\varepsilon_s^{x=1} - \varepsilon_\infty^x}{1 - \omega^2/\omega_{x=1}^2 - i\omega\Gamma/\omega_{x=1}^2} \qquad (1)$$

where ε_s^x, ε_∞^x are the low and high frequency dielectric constants at alloy fraction x. The angular frequency of the GaAs-like (InAs-like) TO phonon is $\omega_{x=1}(\omega_{x=0})$. The damping rate was assumed to be $\Gamma = 0.06 \text{ ps}^{-1}$ for both InAs-like and GaAs-like TO phonon modes [20]. In order to estimate the thickness of semiconductor through which the emitted THz must propagate, we calculated the maximum THz electric field from each 'slice' parallel to the surface. Taking the mean of this distribution results in a weighted propagation thickness of $\sim 0.5\ \mu m$. Assuming that the emitted THz radiation is collected in the reflection geometry (to minimise absorption and dispersion in the semiconductor material [6]) $0.5\ \mu m$ is a reasonable estimate of the propagation distance of THz radiation in an InGaAs photoconductive switch. We therefore propagate E_{THz} through this thickness of semiconductor, and into free space, resulting in a characteristic reduction in spectral amplitude of emitted THz radiation close to a TO phonon mode, and an enhancement just above the frequency of an LO phonon (as seen in Figs. 1–3).

2.3. Laser parameters

The simulation uses incident pulse parameters characteristic of current ultra-short mode-locked lasers (i.e. a Gaussian spatial and temporal shape, and a transform-limited Gaussian energy distribution). For the case of a 10 fs Ti:sapphire laser (with central wavelength $\lambda = 800$ nm, $\Delta\lambda = 80$ nm, typical beam power $P_{\text{exp}} = 400$ mW and a repetition rate $R = 75$ MHz) we use a simulation power of 10 μW and a Gaussian spot of standard deviation $\sigma_{x,y} = 0.5\ \mu m$ in order to obtain the same photon flux as experimentally achievable. While amplified Er:fibre lasers have been demonstrated with pulse durations of 65 fs ($\lambda = 1550$ nm, $\Delta\lambda > 100$ nm, $P_{\text{exp}} = 110$ mW, $R = 67$ MHz) [5], sub-30 fs pulses widely tunable over the wavelength range 1130–1950 nm may be generated by coupling such Er:fibre laser light into a highly non-linear fibre [21]. For excitation around 1.55 μm we use $P = 6$ μW and $\sigma_{x,y} = 0.5\ \mu m$, chosen to give the same photon flux as for the Ti:sapphire, so that a comparison between $In_{0.53}Ga_{0.47}As$ switches excited by 1.55 μm radiation, and GaAs excited by 800 nm can be made in Section 3. With the aim of providing a quick reference to the laser parameters used we refer below to the 10 fs, $\lambda = 800$ nm Ti:sapphire just described as laser A, and the 65 fs $\lambda = 1.55$ μm Er:fibre as laser B.
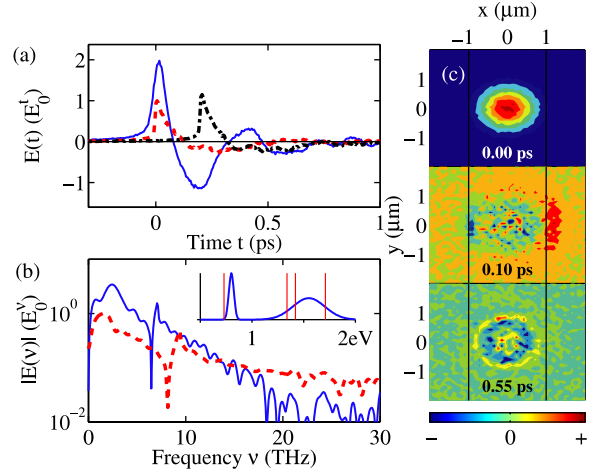

Fig. 1. (Colour online) (a) Simulated E_{THz} for GaAs (dashed line) and InP (dash-dotted line, offset in time by $+0.2$ ps for clarity) photoconductive switches excited by laser A, and InAs (solid line) excited by laser B. Both InP and InAs have a larger peak E_{THz} than GaAs. (b) Fourier transform of $E_{\text{THz}}(t)$ from (a), for InAs (solid) and GaAs (dashed line). The spectrum for InP (not shown) is substantially the same as that for GaAs (with its TO phonon absorption at 9.2 THz). (Inset) Schematic energy distributions of a transform-limited 65 fs pulse at $\lambda = 1.55$ μm (0.8 eV) and a 10 fs pulse at $\lambda = 800$ nm (1.55 eV). Vertical lines at 0.73, 1.34, 1.42 and 1.71 eV, respectively indicate E_Γ for $In_{0.53}Ga_{0.47}As$, InP and GaAs, and E_L for GaAs. (c) Change in electron density between simulation time steps in the plane of the surface ($x-y$), averaged over the depth z (see text for discussion). The black lines at $x = -1$ and 1 μm mark the positions of the cathode and anode.

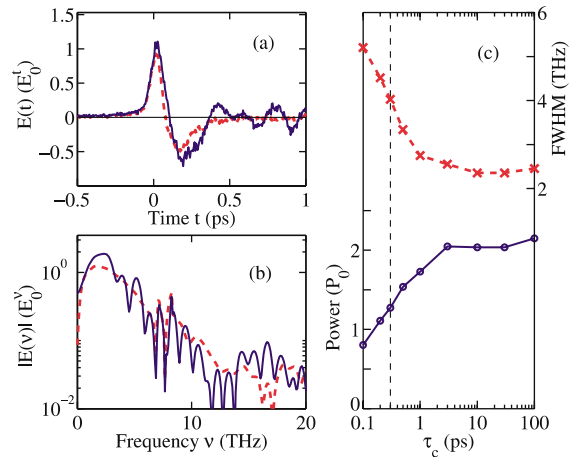Fig. 2. (Colour online) (a) Simulated E_{THz} for $In_{0.53}Ga_{0.47}As$ with $\tau_c = 100$ ps (solid line) and $\tau_c = 0.3$ ps (dashed line), using 65 fs pulses with laser B's parameters. (b) Fourier transform of (a). In (c) the power (circles) and FWHM (crosses) are plotted for $\tau_c = 0.1 - 100$ ps, showing a significant reduction in power and a bandwidth increase as τ_c decreases below 1 ps. The power is normalized to that of GaAs with $\tau_c = 100$ ps (excited by laser A), P_0. The dotted vertical line indicates $\tau_c = 0.3$ ps, used in subsequent figures.

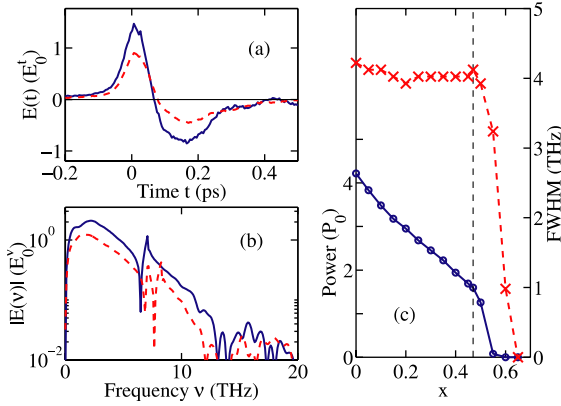Fig. 3. (Colour online) (a) and (b) Simulated E_{THz} for InAs (solid lines) and In$_{0.53}$Ga$_{0.47}$As (dashed lines) with $\tau_c = 0.3$ ps and excited by 65 fs, $\lambda = 1.55$ μm pulses from laser B. (c) Power (circles) and FWHM (crosses) of simulated E_{THz} as a function of x. The dotted vertical line indicates $x = 0.47$.

3. Simulation results

In Fig. 1, we compare the simulated E_{THz} for InP and GaAs photoconductive switches excited by 10 fs pulses from laser A with that obtained for InAs excited by 65 fs pulses from laser B. These parameters were chosen to enable a comparison between THz systems based on current state-of-the-art lasers. In order to enable a comparison between the results presented, we normalize E_{THz} in the time and frequency domains to the peak simulated values for a GaAs photoconductive switch excited by laser A (with carrier trapping time $\tau_c = 100$ ps), denoted E_0^t and E_0^v, respectively. Similarly, the emitted THz power (defined as the square of $E_{THz}(t)$ integrated over all times) is normalized to P_0, the power for the GaAs emitter.

The peak value of E_{THz} for InAs is larger than for GaAs, despite the Er:fibre laser's power being lower than that of the Ti:sapphire (the photon flux is the same for both lasers). This can be attributed in part to a higher fraction of incident photons having above-bandgap energy. As the inset of Fig. 1 indicates, almost 100% of photons from laser B have energy greater than E_Γ(InAs) = 0.35 eV, while the above-bandgap fraction for laser A is smaller ($\sim 80\%$). The fact that InAs has a lower effective mass in the Γ-valley than GaAs also contributes to the power increase. Qualitatively, a smaller effective mass produces a larger mobility $\mu = e\tau/m^*$, which should result in a larger transient current and, therefore, power. However, this argument neglects changes in the carrier scattering time τ, and we return to this point in Section 3.3.

Turning now to E_{THz} for InP, we observe a slightly greater peak time-domain and spectral amplitude than for GaAs, despite the larger m_Γ^* (lower mobility) of InP. This is again related to the energy distribution of the incident infrared pulses. Defining the excess energy of the incident

pulse as $\Delta = E_\gamma - E_\Gamma$ we see that $\Delta = 0.21$ eV for InP, while $\Delta = 0.13$ eV for GaAs. A greater percentage of incident photons are, therefore, absorbed in InP ($\sim 91\%$) than GaAs (80%), contributing to a larger E_{THz}.

The simulated E_{THz} for InAs exhibits an extra oscillatory component after $t = 0.30$ ps, due to the onset of charge–density oscillations that can radiate THz radiation. These plasma-type oscillations can be observed directly in the simulation as a change in electron density between time steps (Fig. 1(c)). At $t = 0.00$ ps the rapid increase in electron density is due to photoexcitation, and produces the first positive peak in E_{THz}. By $t = 0.10$ ps there is an increased electron density at the anode, while the first negative peak in E_{THz} is at $t = 0.2$ ps (Fig. 1(a)), and is primarily a result of the rapid momentum scattering of electrons. The subsequent change in E_{THz} for $t > 0.3$ ps can be identified as resulting from circular regions of altering charge density (Fig. 1(c), $t = 0.55$ ps). Plasma oscillations have been observed previously in the simulation of THz emission from InAs surfaces [12], and become less noticeable as $x \rightarrow 1$ due to GaAs's lower mobility.

3.1. Carrier trapping time

Higher bandwidth terahertz emission can be achieved by introducing defects into a semiconductor using a technique such as high energy ion implantation, or low-temperature (LT) semiconductor growth. In both cases, carriers are trapped on sub-picosecond time scales, with carrier trapping times τ_c as short as 550 fs in LT-In$_{0.3}$Ga$_{0.7}$As (Ref. [9]) and 300 fs in In$_{0.53}$Ga$_{0.47}$As implanted with 2 MeV Fe ions [22]. When τ_c becomes comparable with the duration of a single-cycle THz pulse ($\tau \lesssim 1$ ps) bandwidth improvements can be observed. This effect may be modelled using an exponential reduction in the photoexcited carrier density [13], with a time constant τ_c.

In Fig. 2, we present the simulated THz electric field E_{THz} and calculated spectra for In$_{0.53}$Ga$_{0.47}$As excited by 65 fs pulses of 1.55 μm centre wavelength light, as a function of carrier trapping time. At shorter values of τ_c the negative peak in E_{THz} arrives earlier, creating an increase in the spectral full-width-at-half-maximum (FWHM). This trend can be seen in Fig. 2(c): when $\tau_c \lesssim 1$ ps there is a rapid increase in FWHM at the cost of a reduced power, where the power is defined as $E_{THz}^2(t)$ summed over all simulation times. In the following we chose a value of $\tau_c = 0.3$ ps, achievable experimentally [22].

3.2. Varying alloy fraction at $\lambda = 1.55$ μm

With the intention of optimizing the semiconductor for excitation at 1.55 μm we modelled the THz emission from In$_{1-x}$Ga$_x$As at alloy fractions x in the range $0 \leq x \leq 0.7$. The results of this set of simulations are shown in Fig. 3. The emitted power increases towards InAs to over four times larger than that of GaAs excited by laser A, while

the FWHM remains constant. When $x \gtrsim 0.45$ both the power and FWHM drop dramatically, since the excess incident pulse energy Δ becomes small and then negative, and fewer photoexcited carriers are created.

While these results should be relatively straightforward to verify experimentally, the density and kinetic energy of photoexcited carriers alter significantly when x is varied and λ kept constant. To try to assess better how the material choice alters THz emission (independent of the laser's parameters) we performed a further set of simulations at constant excess excitation energy Δ, as reported in Section 3.3.

3.3. Varying alloy fraction at constant excess pulse energy Δ

Simulations were run over the full range of alloy fraction x with $\Delta = 0.07$ eV and photoexcited carrier density. Pulsed Er:fibre lasers widely tunable in the range 1130–1950 nm (1.1–0.64 eV) have been recently developed [21], which should allow experimental studies of this kind over a significant range of alloy fraction ($0.37 \lesssim x \lesssim 0.77$).

As Fig. 4(a) shows, the emitted THz power increases towards $x = 0$, as found in Section 2. By extracting the total carrier momentum scattering time τ from the simulation (summed over all scattering mechanisms, averaged over all electrons in the Γ valley, and taken at $t = 0.00$ ps) we estimate the high-field electron mobility $\mu(x) \simeq e\tau(x)/m_\Gamma^*(x)$. The relative increase in $\mu(x)$ towards InAs is comparable

Fig. 4. (Colour online) (a) Power (solid lines) and FWHM (dashed lines) of simulated THz electric field from In$_{1-x}$Ga$_x$As ($\tau_c = 0.3$ ps), for incident pulse durations of 10 fs (crosses), 65 fs (triangles), and 100 fs (squares). The photon energy above the bandgap and the incident photon density were kept constant as the alloy fraction x was varied. (b) The average Γ valley electron mobility (solid line) extracted from the simulation (see text for description), can be compared with the (low carrier energy) hall mobility (dashed line). The time t_s in which the applied electric field becomes screened (squares) increases towards GaAs.

with the enhancement in experimental low-field mobility (Fig. 4(b)), and results from a decrease in both the carrier–carrier and carrier–LO phonon scattering rates.

Shortly after the peak intensity of the incident pulse the electric field applied across a photoconductive switch is completely screened by the build-up of the THz-emitting dipole. This occurs in a characteristic screening time $t_s \sim 100$ fs for a semi-insulating GaAs photoconductive switch [14]. By calculating the electric field at the incident spot position (x, $y = 0$ µm) as a function of time, it is possible to extract the screening time t_s, defined as the time at which the electric field becomes zero. Fig. 4(b) indicates that t_s increases as the Ga alloy fraction $x \to 1$, as a result of the lower electron mobility. It should be noted that a shorter screening time does not necessarily mean a reduction in the THz power emitted: a higher mobility can produce both a lower t_s and a greater power.

This simulation set was repeated for incident pulse durations of 10 and 100 fs. In the 10 fs case the total power emitted (Fig. 4(a)) is smaller than for 65 fs across the entire range of x, as fewer carriers are photoexcited. However, for 100 fs the power is again lower than the 65 fs case, because when the later carriers are photoexcited the electric field is already partly screened. How the THz power and bandwidth alter as a function of incident pulse duration was discussed for semi-insulating GaAs in Ref. [14]. The FWHM of the 100 fs spectra are lower than those of the 10 and 65 fs simulations, owing to the slow rise in E_{THz}. Somewhat counterintuitively, the 10 fs spectra do not have greater FWHM than the 65 fs over the whole range of x. This can be explained by noting that the FWHM measures the width of the spectrum, and not the high-frequency spectral tail. Thus while greater spectral amplitude is obtained at high frequencies for 10 fs excitation (e.g. Fig. 1(b)), the amplitude at low-frequency (which dominates the FWHM) is larger at incident pulse durations of 65 fs.

4. Conclusion

In summary, we have simulated the terahertz emission from In$_{1-x}$Ga$_x$As photoconductive switches over the entire alloy fraction range $0 \leq x \leq 1$. Two methods for increasing the THz power from photoconductive switches were identified. Firstly, a larger electron mobility resulted in a larger THz power as the Ga alloy fraction was decreased. This suggests that semiconductors with high mobility/low effective mass may be used to improve THz power, for example InAs (($m_\Gamma^* = 0.022 m_e$)) or InSb (($m_\Gamma^* = 0.014 m_e$)). Experimentally, a high resistivity or semi-insulating InAs may be required to produce a photoconductive switch with a low dark current. Secondly, increased THz power can be obtained by judicious choice of incident pulse energy, so that the majority of photons are absorbed.

The spectra calculated from the simulation indicate that InAs photoconductive switches have greater power than
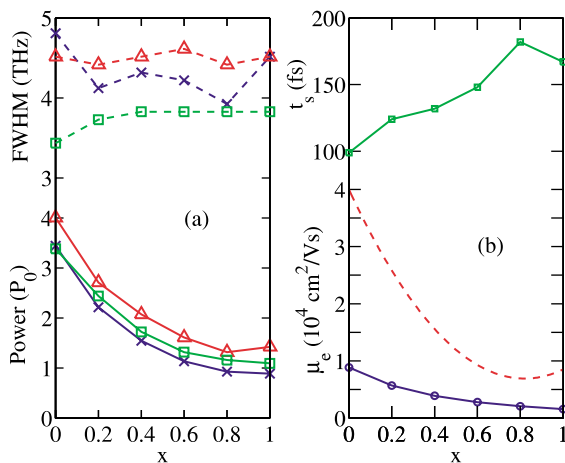
GaAs over the frequency range 0–15 THz. At higher frequencies, the initial rise in E_{THz} (dominated by the incident pulse duration) governs the amplitude. This result seems to suggest that an InAs/65 fs Er:fibre laser setup should produce THz pulses that are at least as powerful as those from 10 fs Ti:sapphire/GaAs setups.

Acknowledgements

References

[1] J.G. Rivas, M. Kuttge, P.H. Bolivar, H. Kurz, J.A. Sanchez-Gil, Phys. Rev. Lett. 93 (25) (2004) 256804.

[2] M.B. Johnston, L.M. Herz, A.L.T. Khan, A. Köhler, A.G. Davies, E.H. Linfield, Chem. Phys. Lett. 377 (1–2) (2003) 256.

[3] T. Muller, W. Parz, G. Strasser, K. Unterrainer, Phys. Rev. B 70 (15) (2004) 155324.

[4] P. Smith, D. Auston, M. Nuss, IEEE J. Quantum Electron. 24 (2) (1988) 255.

[5] F. Tauser, A. Leitenstorfer, W. Zinth, Opt. Express 11 (6) (2003) 594.

[6] Y.C. Shen, P.C. Upadhya, E.H. Linfield, H.E. Beere, A.G. Davies, Appl. Phys. Lett. 83 (2003) 3117.

[7] P.K. Benicewicz, A.J. Taylor, Opt. Lett. 18 (16) (1993) 1332.

[8] T. Hattori, S. Arai, K. Tukamoto, Jpn. J. Appl. Phys. Part 1 43 (11A) (2004) 7546.

[9] C. Baker, I.S. Gregory, W.R. Tribe, I.V. Bradley, M.J. Evans, M. Withers, P.F. Taday, V.P. Wallace, E.H. Linfield, A.G. Davies, M. Missous, Appl. Phys. Lett. 83 (20) (2003) 4113.

[10] M. Suzuki, M. Tonouchi, Appl. Phys. Lett. 86 (20) (2005) 051104.

[11] J. Mangeney, L. Joulaud, P. Crozat, J.-M. Lourtioz, J. Decobert, Appl. Phys. Lett. 83 (26) (2003) 5551.

[12] M.B. Johnston, D.M. Whittaker, A. Corchia, A.G. Davies, E.H. Linfield, Phys. Rev. B 65 (16) (2002) 165301.

[13] J. Lloyd-Hughes, E. Castro-Camus, M.D. Fraser, C. Jagadish, M.B. Johnston, Phys. Rev. B 70 (2004) 235330.

[14] E. Castro-Camus, J. Lloyd-Hughes, M.B. Johnston, Phys. Rev. B 71 (19) (2005) 195301.

[15] I. Vurgaftman, J.R. Meyer, L.R. Ram-Mohan, J. Appl. Phys. 89 (11) (2001) 5815.

[16] NSM semiconductor archive. URL http://www.ioffe.rssi.ru/SVA/NSM/Semicond/.

[17] J. Groenen, R. Carles, G. Landa, C. Guerret-Piecourt, C. Fontaine, M. Gendry, Phys. Rev. B 58 (16) (1998) 10452.

[18] S. Zollner, S. Gopalan, M. Cardona, J. Appl. Phys. 68 (4) (1990) 1682.

[19] J. Shan, T.F. Heinz, Ultrafast Dynamical Processes in Semiconductors, Springer, Berlin, 2004. pp. 1–56 (chapter 1).

[20] P.Y. Yu, M. Cardona, Fundamentals of Semiconductors, third ed., Springer, Berlin, 2003.

[21] F. Tauser, F. Adler, A. Leitenstorfer, Opt. Lett. 29 (5) (2004) 516.

[22] C. Carmody, H.H. Tan, C. Jagadish, A. Gaarder, S. Marcinkevicius, Appl. Phys. Lett. 82 (22) (2003) 3913.